LASER & PHOTONICS REVIEWS
www.lpr-journal.org

Polarized Light Backscattering From Turbid Media: Why Do Rayleigh Scatterers Preserve Linear Polarization More Than Circular Polarization?

Michael D. Singh and Alex Vitkin*

Linear and circular degree of polarization (DOP) trends are studied in microsphere suspensions ranging from the Rayleigh regime (sphere diameter $<< \lambda$) to larger sizes (sphere diameter $\approx \lambda$) through experimental measurements and computational modeling. In doing so, linkages between single-scattering and multiple-scattering effects of polarized light are investigated to gain mechanistic insight into the question of why linear DOP is often greater than circular DOP when light is backscattered from turbid media comprised of Rayleigh-regime scatterers – a phenomenon which is not yet well understood. The findings of the study may indicate that linear DOP is enhanced by Rayleigh scatterers due to 1) increased direct backscattering pathways (via mirror-like large-angle reflections from scatterers) and 2) increased arc-like-pathway scattering along the plane that is perpendicular to the incident linear polarization vector. Both 1) and 2) result in higher co-linear intensity, also resulting in overall higher linear DOP than circular DOP.

1. Introduction

Backscattered polarized light exhibits interesting depolarization effects which are strongly influenced by the average "scatterer size" of the interacting medium.[1] Depolarization refers to the decorrelation between electric field waves which comprise a beam of light,[2] and "scatterer size" quantifies the average size of scattering centres in a medium.[3] Optical sensitivity to particle or scatterer size has become an important research issue due to its utility in applications including cell and protein sizing (microfluidics),[4] soil characterization in the agriculture industry,[5] and epithelial cancer detection.[6,7] Thus, polarized light scattering is a subject of active investigation.

In a seminal study several decades ago, MacKintosh et al.[8] performed *degree of polarization* (DOP) measurements of backscattered light from suspensions of polystyrene microspheres. The DOP is often used to study depolarization effects, quantifying the fraction of light that remains polarized and is calculated as DOP = 1 – depolarization. In that study, it was found that linear depolarization rates differ from circular depolarization rates, depending on the average sphere diameter of the medium. Specifically, it was found that:

Circular DOP > linear DOP for suspensions of larger spheres (sphere diameter $\approx \lambda$)

Linear DOP > circular DOP for suspensions of smaller spheres (sphere diameter $<< \lambda$, i.e., the Rayleigh regime)

These findings have been corroborated by several follow-up studies, both experimentally and numerically, including our own.[1,9–20]

The differences in linear and circular DOP are thought to arise, at least in part, from the different "geometrical" depolarization effects for backscattered linearly and circularly polarized light. Specifically, linear polarization vectors can be geometrically rotated to any orientation in the wavefront plane ranging continuously through 0°–360° (with 0° = vertical, 90° = horizontal, etc.), whereas circular polarization vectors may only be geometrically reorientated between right-handed and left-handed circular polarization states.[1,19,21,22] It is thus posited that linearly polarized light will typically depolarize more readily and is the underlying reason for higher circular DOP in various media (originally termed "circular polarization memory"),[8] which tends to be observed in media comprised of larger scatterers (i.e., "Mie regime" media).[8,23,9] It is therefore curious that linear polarization can actually be better preserved than circular polarization in some media, which tends to occur in media comprised of Rayleigh-regime scatterers, despite the additional degrees of rotational

M. D. Singh, A. Vitkin
Department of Medical Biophysics
University of Toronto
Toronto, ON M5G 1L7, Canada
E-mail: michaeldhillon.singh@mail.utoronto.ca
A. Vitkin
Department of Radiation Oncology
University of Toronto
Toronto, ON M5T 1P5, Canada
A. Vitkin
Princess Margaret Cancer Centre
University Health Network
Toronto, ON M5G 2C4, Canada

The ORCID identification number(s) for the author(s) of this article can be found under https://doi.org/10.1002/lpor.202501487

DOI: 10.1002/lpor.202501487

freedom and thus scrambling mechanisms of linear polarization vectors.

Many of the studies on polarized light scattering in turbid media have been performed in the context of *bio-polarimetry* (i.e., polarization measurements of biological tissues to extract useful biophysical information),[24,25] since biological tissues are heterogeneous and hence turbid.[26] In particular, depolarization signatures have been shown to provide information on the optical scattering and physical properties of tissues, which may become useful in detecting various diseases (e.g., scatterer size changes have been related to cancer progression).[7,27–35] Indeed, due to the consistent finding in microsphere suspensions (and other non-tissue media) of the association between 1) higher circular DOP (relative to linear DOP) and larger scatterers, and 2) higher relative linear DOP and small Rayleigh-like scatterers,[1,–19] when these depolarization behaviours are observed in biological tissues, authors often interpret them as indicators of scatterer size. This is particularly true for the observation of linear DOP > circular DOP in tissues, prompting suggestions that the tissues are likely composed of small Rayleigh-like scatterers.[29,36–39] Interestingly though, to the best of our knowledge, despite the consistency of these depolarization relationships in phantoms (i.e., non-biological media) and their usage to interpret tissue data, we still lack a clear mechanistic understanding of *how* linear DOP becomes greater than circular DOP in backscattered light as scatterer size decreases into the Rayleigh regime.

Thus, through both experimental measurements and computational modeling, we investigate the linkages between single-scattering and multiple-scattering effects of polarized light, and how they are influenced by changes in scatterer size, to better understand linear and circular DOP differences in Rayleigh and non-Rayleigh media. To do so, we examine how scatterer size affects the 3D single-scattering directionality of spheres (i.e., polarization-sensitive intensity distributions), and how such single-scattering directionality then modulates multiple scattering pathways of backscattered light. Since circular polarization vectors are rotationally symmetrical in the wavefront plane, as opposed to bisymmetrical (two lines of symmetry) linear polarization vectors, there are geometrical effects to consider when comparing multiple scattering pathways of the two polarization states. Linear and circular DOP values depend on the relative intensities of parallel and orthogonal polarization states; thus, these geometrical effects become important since they significantly influence parallel and orthogonal polarization intensity fractions. Notably, to aid in this investigation, we employ modified Stokes DOP formulae to track the relative fractions of helicity-flipped/co-linear polarization and helicity-preserved/cross-linear polarization intensities, in addition to the magnitude of DOP.

2. Methods

2.1. Degree of Polarization Calculations

Circular DOP is typically calculated via Stokes calculus as

$$\mathrm{DOCP}_o = \sqrt{(S_3)^2}/S_0 = \sqrt{(R-L)^2}/(R+L) \quad (1)$$

where "R" and "L" are right-circular and left-circular polarization intensity, respectively[40] (note that S_0 can be the sum of any two orthogonal states). However, it can also be expressed as a signed value, whereby circular DOP is calculated as $(R-L)/(R+L)$.[40] If, say, right circular polarization is the incident state, circular DOP is calculated as $(RR-RL)/(RR+RL)$, where "RL" is incident right-circular polarization and measured left-circular polarization (and "RR" = right-circular incident and right-circular measured). Thus, it follows that circular DOP can be expressed as

$$\mathrm{DOCP} = (HP-HF)/(HP+HF) \quad (2)$$

where "HP" is helicity-preserved intensity (e.g., right-circular incident and right-circular measured) and "HF" is helicity-flipped intensity (e.g., right-circular incident and left-circular measured). Indeed, this is how circular DOP is often calculated, such as in refs. [8,41,15,42]. Thus, circular DOP is positive when helicity-preserved intensity > helicity-flipping intensity, and negative when helicity-flipped intensity > helicity-preservation intensity. Equation (2) thus provides the same magnitude that would be calculated using the conventional circular DOP calculation; however, it also encodes the helicity response into the sign. This becomes useful when characterizing the scattering properties of a turbid medium, particularly particle/scatterer size.[43]

Interestingly, linear DOP can also be calculated in a similar manner. The conventional Stokes calculation for linear DOP is

$$\mathrm{DOLP}_o = \sqrt{(S_1)^2+(S_2)^2}/S_0 = \sqrt{(H-V)^2+(45^+-45^-)^2}/S_0 \quad (3)$$

for any given incident polarization state. Thus, say, for incident vertically polarized light, the linear DOP becomes $\sqrt{(VH-VV)^2+(V45^+-V45^-)^2}/S_0$. For purely scattering, non-birefringent media, such as microsphere suspensions, the second term in the numerator, $(V45^+-V45^-)$, becomes zero since the measured linear 45^+ intensity must be the same as linear 45^- intensity for incident vertically polarized light (there is no mechanism which will cause the non-birefringent medium to scatter linear 45^+ differently than linear 45^- since they are both effectively treated the same with respect to the incident vertical linear polarization). Therefore, linear DOP can be expressed as $\sqrt{(VH-VV)^2}/(VH+VV)$ (again, note that the denominator S_0 is the sum of any two orthogonal states). To have a signed value, the above equation becomes $(VH-VV)/(VH+VV)$. It follows that linear DOP can then be expressed as

$$\mathrm{DOLP} = (\perp - \parallel)/(\perp + \parallel) \quad (4)$$

where $\perp$ is cross-linear polarization intensity (e.g., vertical linear incident and horizontal linear measured), and $\parallel$ is co-linear polarization intensity (e.g., vertical linear incident and vertical linear measured). Indeed, this is how linear DOP is often calculated, such as in refs. [44–48].

Thus, Equation (4) yields a linear DOP with the same magnitude as given by the conventional calculation; however, the sign encodes the preponderance of cross-linear intensity (positive sign) or co-linear intensity (negative sign). Akin to the signed circular DOP equation above (Equation (2)), this signed linear

DOP equation offers additional information compared to the magnitude-only linear DOP value. For example, media of small scatterers are known to backscatter more co-linear polarization intensity than cross-linear polarization intensity.[8,10,49,50,51] (Co-linear backscattering is analogous to helicity-flipped backscattering since they both occur upon mirror-like reflections).

Important to note, the conventional circular and linear Stokes DOP equations (Equations (1) and (3)) are agnostic to the incident state of the light, whereas the modified DOP equations (Equations (2) and (4)) yield signed DOP measurements which are relative to the incident state of light. Equations (2) and (4) are thus advantageous since they may offer the same information in magnitude as the conventional Stokes DOP equations; however, they also indicate which of the orthogonal states are dominant via the sign (e.g., a negative sign indicates that co-linear > cross-linear, or that helicity-flipped > helicity-preserved). The latter yields interesting information on scatterer size, as will be shown below, and enables fair comparison between linear and circular DOP since both take on negative values upon direct backscatter events such as specular reflection and remain positive otherwise.

2.2. 3D Single Scattering Intensity Distributions

The angular distribution of singly-scattered polarized light can be calculated by multiplying the Mueller matrix of a sphere with a given Stokes vector:

$$S_{out}(\theta) = M_s(\theta) \times S_{in} \tag{5}$$

$$\begin{bmatrix} I_{out}(\theta) \\ Q_{out}(\theta) \\ U_{out}(\theta) \\ V_{out}(\theta) \end{bmatrix} = \begin{bmatrix} M_{11}(\theta) & M_{12}(\theta) & 0 & 0 \\ M_{12}(\theta) & M_{11}(\theta) & 0 & 0 \\ 0 & 0 & M_{33}(\theta) & M_{34}(\theta) \\ 0 & 0 & -M_{34}(\theta) & M_{33}(\theta) \end{bmatrix} \times \begin{bmatrix} I_{in} \\ Q_{in} \\ U_{in} \\ V_{in} \end{bmatrix} \tag{6}$$

M_s represents the Mueller matrix of a single scatterer, S_{out} and S_{in} are the scattered and incident Stokes vectors, respectively, and θ represents the scattering angle as depicted in **Figure 1**. The matrix elements are calculated using Mie theory, whose expressions are derived and shown in detail in ref. [52]. Briefly, the Mueller matrix relationship in Equation (6) is derived by relating the incident and scattered field amplitudes of light through the "scattering amplitude function" of a single spherical particle:

$$\begin{pmatrix} E_{\parallel s}(\theta) \\ E_{\perp s}(\theta) \end{pmatrix} = \frac{e^{-ikr+ikz}}{ikr} \begin{pmatrix} S_2(\theta) & S_3(\theta) \\ S_4(\theta) & S_1(\theta) \end{pmatrix} \begin{pmatrix} E_{\parallel i} \\ E_{\perp i} \end{pmatrix} \tag{7}$$

where $E_{\parallel}$ and $E_{\perp}$ are orthogonal field amplitudes (subscript "s" and "i" denote scattered and incident fields, respectively), the matrix of S_1, S_2, S_3, and S_4 is the scattering amplitude function of the spherical particle, and $\frac{e^{-ikr+ikz}}{ikr}$ is the wave equation ("k" is the wave number, "r" is the radial distance). Notably, for spheres, S_3 and S_4 equal zero in Equation 7 due to symmetry relations, giving rise to $M_{11} = M_{22}$ and $M_{33} = M_{44}$ equivalencies. The reader is referred to the works of Van De Hulst (Ch. 4 and Ch. 5),[53] Bohren and Huffman (Ch. 3 and Ch. 4).[3] and Raković et al.[19] for the rigorous mathematical details derived from first principles.

In order to calculate the scattering intensity in three-dimensions, as seen in **Figure 2**, the scattering plane was rotated about the Z-axis (centred at X,Y = 0,0) in 5° increments along the ϕ direction shown in Figure 1, and for each incremental rotation, the scattered intensity of each polarization state, $S_{out}(\theta)$, is calculated using Equations (5) and (6). Note that the incident linear polarization orientation changes with respect to the scattering plane at each ϕ rotational increment (hence the incident Stokes vector, S_{in}, changes), whereas the incident circular polarization orientation remains constant due to its azimuthal symmetry.

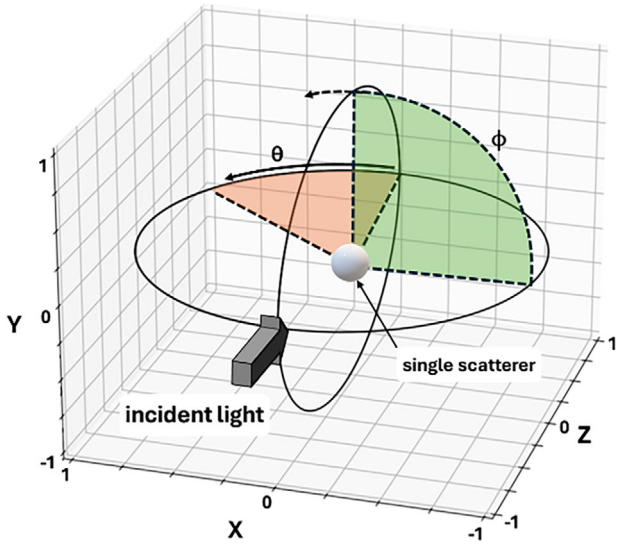

Figure 1. Depiction of the coordinate system for 3D single-scattering intensity distributions. The scattering angle θ spans 360° in the counter-clockwise direction (viewing from above) in the X-Z (Y = 0) plane, as depicted by the orange-shaded region. The scattering plane is incrementally rotated along the ϕ direction about the Z-axis (centered at X,Y = 0,0) in order to generate 3-D intensity distributions; see related text for details.

The scattered circular polarization intensity is calculated as V_{out}/I_{out} for each scattering angle θ, at each ϕ rotation, with $S_{in} = [1, 0, 0, 1]^T$ (incident right-circular polarization) using Equation (6); similarly, the scattered linear polarization is calculated as Q_{out}/I_{out} with $S_{in} = [1, -1, 0, 0]^T$ (incident linear vertical polarization). The following input parameters were used for Mie scattering calculations: incident light wavelength λ = 632.8 nm, scatterer refractive index n_s = 1.59 (polystyrene), and host refractive index n_m = 1.33 (water).

2.3. Microsphere Suspensions

Monodispersed polystyrene microspheres (Bangs Laboratories, Inc) with diameters of 0.03, 0.50, and 1.04 µm were suspended in deionized water to yield a reduced scattering coefficient of $\mu_s' = 3.4\ cm^{-1}$ (this was the highest available turbidity for the 0.03 µm microsphere suspension from the manufacturer; thus, the other two suspensions were set to match that). The 0.03, 0.50, and 1.04 µm spheres had scattering efficiencies (Q), g-factors (g), and concentrations (ρ) of [Q =6.38 × 10^{-5}, g =0.007, ρ =7.50 × 10^3 spheres µm^{-}3], [Q =0.77, g =0.82, ρ =1.50 spheres µm^{-3}], and [Q =2.73, g =0.92, ρ =0.16 spheres µm^{-3}], respectively. These Mie values were determined using the calculator in ref.[54] with the following input parameters: incident light wavelength λ = 632.8

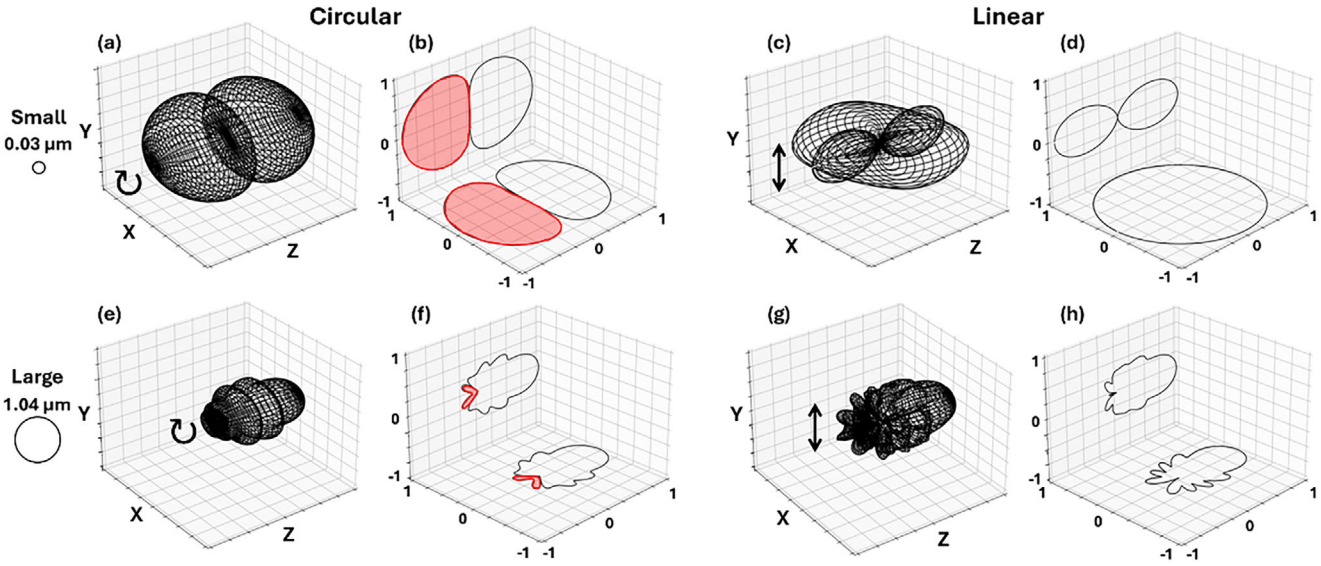

Figure 2. a,b,e,f) 3D single-scattering plots of scattered circular polarization intensity (the red-shaded lobes indicate helicity-flipping) and c,d,g,h) scattered linear polarization intensity for a 0.03 μm diameter sphere (top row) and a 1.04 μm diameter sphere (bottom row). Note that the scattered intensities of the 0.03 μm sphere are smaller by 5 orders of magnitude compared to the 1.04 μm sphere (see the scattering efficiency values in the "Microsphere suspensions" paragraph in Methods); this is not visually apparent since each scattering intensity is normalized to 1.

nm, sphere refractive index $n_s = 1.59$, and the host medium refractive index of $n_m = 1.33$ (deionized water).

2.4. Experimental Polarimetric System

The configuration and detailed description of the polarimetric imaging system can be found in ref. [43]. Briefly, a helium-neon laser source at $\lambda = 632.8$ nm was employed, along with an intensified-CCD camera (PI-MAX 3, Princeton Instruments) configured into an exact backscattering $\theta = 180°$ detection scheme using a beam-splitter. The Mueller matrix of the beam-splitter was measured and accounted for in the calculation of each polarimetric image; see ref. [43] for details. Each suspension was contained in a cuvette of 1.1 cm diameter and illuminated by a pencil beam of ~2 mm diameter (full width at half maximum), which was linearly or circularly polarized. The backscattered light was filtered with polarization analyzers to enable detection of a co-linear and cross-linear image (for incident linear polarization) or a helicity-flipped and helicity-preserved image (for incident circular polarization). Vertical illumination of each suspension's exposed liquid surface was performed to avoid the use of a physical window and any potential accompanying artifacts (e.g., multiple reflections between the window and medium, or interference effects).

2.5. Monte Carlo Simulation Platform

The simulation parameters were configured to match the phantom experiment: 10^8 polarized photon packets ($\lambda = 632.8$ nm) were launched into a $1.1 \times 1.1 \times 3$ cm medium of monodispersed 0.03, 0.50, and 1.04 μm spheres, each with a refractive index of 1.59, suspended in a host refractive index of 1.33, and a reduced scattering coefficient of $\mu_s' = 3.4$ cm^{-1}. Additional sphere diameters of 0.20 and 0.75 μm were also simulated for the data in Figure 6. The photons were launched as a 2 mm diameter beam for the data in Figure 5a–f, whereas the photons were launched as a broad beam of diameter 4 cm (to cover the entire face of the medium) for the data in Figure 6; see the Results and Discussion section for details. The specifics of the Monte Carlo simulation platform can be found in refs. [20,55,56].

3. Results and Discussion

3.1. Analysis of 3D Single-Scattering Plots

To gain insight into the backscattering pathways of circularly and linearly polarized light in media composed of different scatterer sizes, we analyze 3D intensity distributions of scattered polarized light from single polystyrene spheres of diameter 0.03 and 1.04 μm. Each sphere diameter has two single-scattering plots showing: 1) scattered circular polarization intensity (from incident circularly polarized light), and 2) scattered linear polarization intensity (from incident linearly polarized light).

The scattered circular polarization intensity distributions are shown in Figure 2a for the 0.03 μm sphere and Figure 2e for the 1.04 μm sphere. The scattered linear polarization intensity distributions are shown in Figure 2c for the 0.03 μm sphere and Figure 2g for the 1.04 μm sphere. 2D projections of each 3D intensity distribution plot are shown on the X-Z plane and Y-Z plane in Figure 2b,f for circular polarization and Figure 2d,h for linear polarization. The red-shaded lobes in Figure 2b,f indicate helicity flipping of circular polarization; the linear polarization plot is not color-coded since the orientation of the scattered light remains vertically polarized (co-linear) and only changes in intensity. Note that the 1.04 μm sphere has a scattering efficiency of Q = 2.73, whereas the 0.03 μm sphere has a scattering efficiency

of $Q = 6.38 \times 10^{-5}$; thus, the scattered intensities of the 0.03 μm sphere are smaller by 5 orders of magnitude, but this is not visually apparent since each scattering intensity is normalized to 1 (e.g., V_{out}/I_{out} and Q_{out}/I_{out}).

3.1.1. Small (0.03 μm) Sphere

For the 0.03 μm sphere, the scattering plots for circular (Figure 2a,b) and linear (Figure 2c,d) polarization both have roughly equal forward-scattering and backward-scattering intensities, as expected for a Rayleigh scatterer.[57] However, the circular polarization plot has rotational symmetry in the wavefront plane (X-Y plane) such that the projected profiles on the X-Z and Y-Z planes are equivalent (Figure 2b), whereas the linear polarization plot has two different axes of symmetry in the wavefront plane such that the projected scattering profiles on the horizontal plane and vertical plane are different (Figure 2d). Also, notice that scattering is isotropic in the X-Z plane, which is the plane perpendicular to the vertically oriented incident linear polarization vector (Figure 2d). Indeed, this is characteristic of Rayleigh scattering due to the induced dipole effect: perpendicular to the incident linear polarization vector, the scattering intensity with respect to scattering angle is ~isotropic, whereas parallel to the incident linear polarization vector, the scattering profile exhibits two lobes with zero intensity at 90° and 270° scattering angles.[57] These zero intensity lobes are well-known because an induced dipole cannot radiate light parallel to the dipole axis.[57]

3.1.2. Large (1.04 μm) Sphere

For the larger 1.04 μm sphere, as expected,[58] there is more forward scattering for both circular (Figure 2e,f) and linear (Figure 2g,h) polarization. Again, it is noted that the circular polarization plot has rotational symmetry in the wavefront plane such that the projected profiles on the X-Z and Y-Z planes are equivalent (Figure 2f). Contrary to the Rayleigh scattering case, the linear polarization plot exhibits much more rotational symmetry in the wavefront plane such that the projected scattering profiles on the X-Z and Y-Z planes are similar (Figure 2h), with slightly increased back-scatter intensity in the X-Z plane, which is perpendicular to the incident linear polarization vector.

3.2. Hypotheses on Multiple-Scattering Derived From the Single-Scattering Plots

As discussed above, the 3-D single-scattering profiles differ for circular and linear polarization, particularly for the small 0.03 μm Rayleigh spheres. Thus, the ratio of helicity-flipping to helicity-preserving intensity for circular polarization (which governs circular DOP; see Equation (2)) must differ from the ratio of co-linear-to-cross-linear intensity for linear polarization (which governs linear DOP; see Equation (4)). To better understand these differences, as was done in our previous study,[20] we define two types of backscattered light in a medium. Type-1: light which has undergone a mirror-like reflection by a scatterer (large-angle backscattering) at some depth in the medium. Type-2: light which is forward-scattered at small angles and redirected along an arc-like pathway into the backward hemisphere of the medium (i.e., without a mirror-like reflection/large-angle backscattering event). Type-1 and type-2 backscattering are depicted in Figures 3a and 4a (red arrows are type-1, blue arrows are type-2).

3.2.1. Circular Polarization

For circularly polarized light, as depicted in **Figure 3a**, type-1 backscattering results in helicity-flipping, which occurs closer to the region of incidence, whereas type-2 backscattering results in helicity-preservation, which occurs further away from the region of incidence (see ref. [55] for details). Also, due to the ϕ rotational symmetry of the circular polarization vector, type-2 backscattering results in helicity-preservation no matter the location of re-emerging light (e.g., along the X, Y, and 45° axes) as shown in Figure 3b – this is different from the linear polarization case as discussed below.

Thus, one expects a distribution of helicity-flipped and helicity-preserved light backscattered from a medium with incident circularly polarized light as depicted in Figure 3c, such that helicity-flipping occurs near the incident region and helicity-preservation occurs (symmetrically) further outside of the incident region (as previously observed).[55] Furthermore, as scatterer size decreases, one would expect stronger helicity-flipped intensity due to the enhanced backward-scattering in small scatterers (mirror-like backward scattering; see Figure 2a,b), and conversely, larger scatterers will induce stronger helicity-preservation intensity due the enhanced forward-scattering (see Figure 2e,f). Indeed, this is a relatively well-observed relationship between circularly polarized light and scatterer size.[10]

3.2.2. Linear Polarization

It has been known for decades that co- and cross-linear polarization images of turbid media illuminated by linearly polarized light exhibit four-lobed patterns, arising from geometrical effects due to type-2 backscattering.[56,59–62] Type-1 backscattering results in co-linear polarization (e.g., akin to reflection from a mirror) as depicted in **Figure 4a**, whereas type-2 backscattering can yield either co-linear or cross-linear polarization depending on the location in which the light returns. As shown in Figure 4b, type-2 backscattering along the planes that are parallel and perpendicular to the incident linear vertical polarization vector results in co-linear polarization, whereas type-2 backscattering along the planes that are at 45° relative to the incident linear vertical polarization vector results in cross-linear polarization (see ref. [60] for a rigorous examination of these geometrical effects).

Thus, one expects a distribution of co-linearly and cross-linearly polarized light backscattered from a medium with incident linear vertical polarization as depicted in Figure 4c. Co-linear polarization is expected to occur near the illumination region and in lobes along the parallel and perpendicular axes (relative to the incident linear vertical vector), whereas cross-linear polarization is expected to only occur in lobes along the 45° axes (relative to the incident linear vertical vector) – as previously

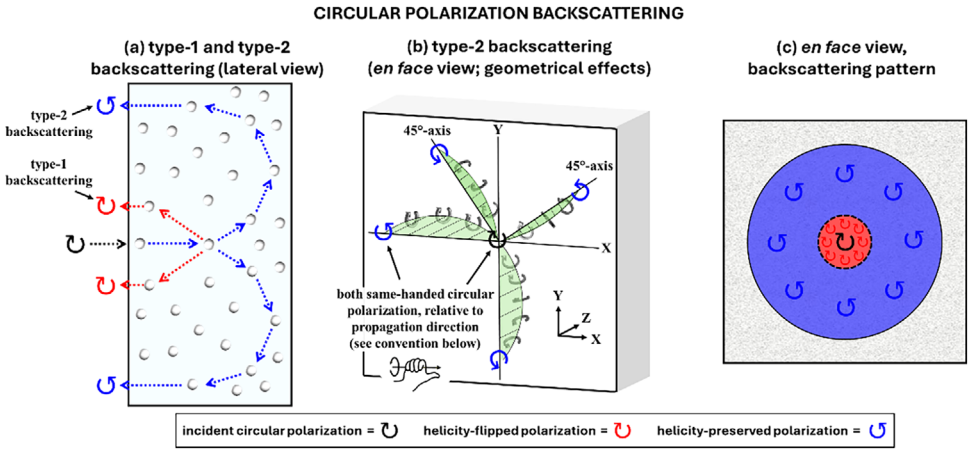

Figure 3. Visualization of the backscattering effects of circularly polarized light. a) Lateral-view depiction of type-1 and type-2 backscattering pathways; type-1 results in helicity-flipping, type-2 results in helicity-preservation. b) *En face* view of type-2 backscattering, showing that type-2 pathways yield helicity-preserved light along all axes (as opposed to the linear polarization case in Figure 4b below). c) Expected distribution of helicity-flipped and helicity-preserved light resulting from an incident circular polarization beam-spot.

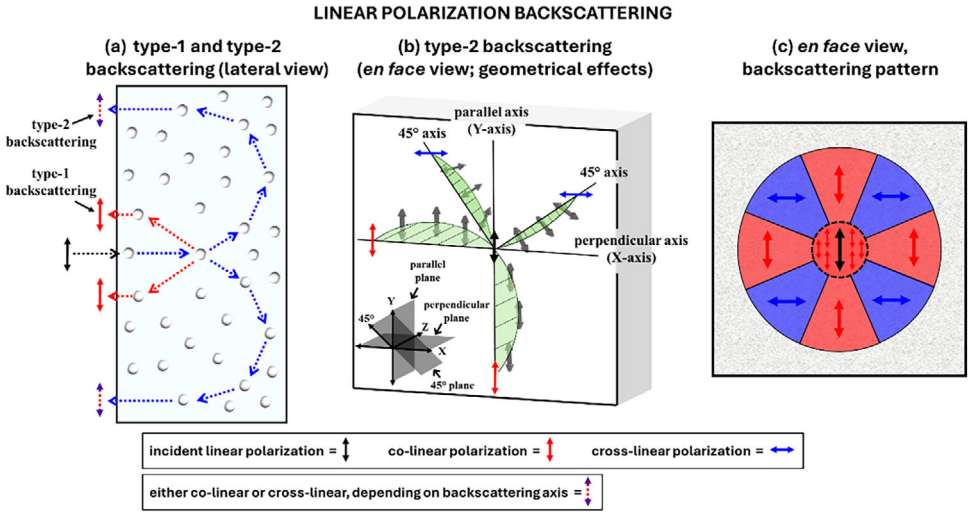

Figure 4. Visualization of the backscattering effects of linearly polarized light. a) Lateral-view depiction of type-1 and type-2 backscattering pathways; type-1 results in co-linear polarization, type-2 can result in either co-linear or cross-linear, depending on the backscattering plane, as shown in b). b) 3D view of type-2 backscattering, showing that type-2 pathways yield co-linear polarization along the parallel axis and perpendicular axis (i.e., parallel or perpendicular to the incident linear polarization vector), and cross-linear polarization results from type-2 pathways along axes which are at 45° with respect to the incident linear polarization vector. c) Expected distribution of co-linear and cross-linear polarization resulting from an incident linear vertical polarization beam-spot.

observed.[56,59–62] Interestingly, notice in Figure 2c,d that, as scatterer size decreases into the Rayleigh regime, two effects occur for scattered linearly polarized light: 1) backscattering is enhanced (as is the case for circularly polarized light), and 2) scattering becomes isotropic in the plane perpendicular to the incident linear vertical polarization vector (X-Z plane), yielding increased side-scattering and forward scattering along this plane. Therefore, small Rayleigh-regime scatterers will enhance co-linear polarization through enhanced type-1 backscattering, but also through enhanced type-2 backscattering along the perpendicular plane. This will give rise to an overall higher linear DOP than circular DOP in Rayleigh scattering media; circular DOP will only be enhanced by higher type-1 backscattering and not type-2 backscattering.

3.3. Degree of Polarization Analysis: Linear Polarization Versus Circular Polarization

Figure 5 shows the circular DOP (a-c, g-i) and linear DOP (d-f, j-l) images of backscattered light from beam-spot-illuminated microsphere suspensions comprised of 0.03, 0.50, and 1.04 μm diameter spheres, each with a matched reduced scattering coefficient of

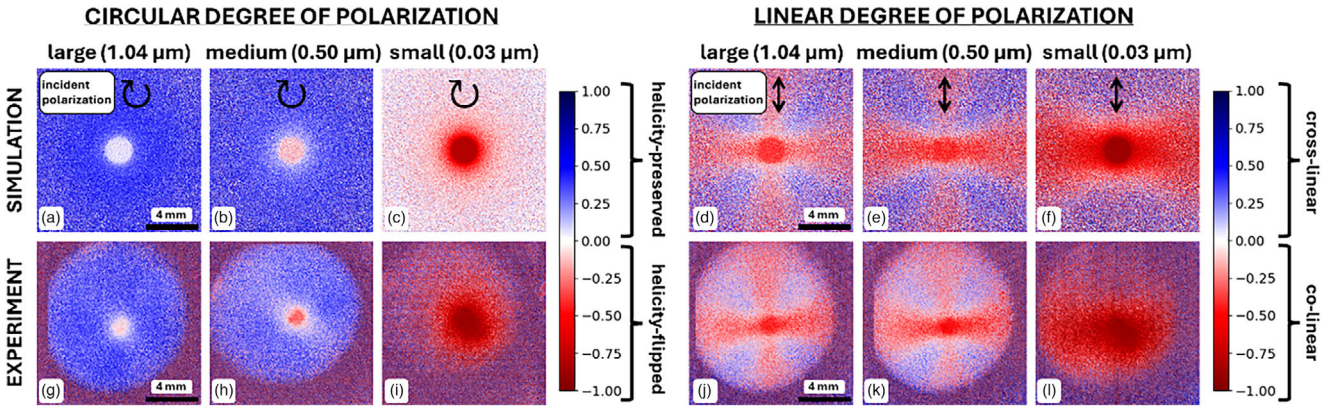

Figure 5. Circular DOP images a-c,g-i) and linear DOP images d-f,j-l) of pencil-beam-illuminated suspensions of 0.03 μm, 0.50 μm, and 1.04 μm microspheres. Simulation images (top row) and experimental images (bottom row) agree well in most instances; for details, see text.

$\mu_s' = 3.4\ \mathrm{cm}^{-1}$; simulation-based images are shown in the top row (a-f) and experimental images are shown in the bottom row (g-l). The experimental images exhibit reasonable agreement with the simulations; note that the experimental images are slightly off-centred due to specular reflection challenges from the surface of each suspension. (Given this good agreement, we will continue our analysis on the simulation images due to their higher clarity.) Note that negative circular DOP values (red-shaded pixels) signify relatively higher helicity-flipping intensity compared to helicity-preservation intensity, according to Equation (2). Similarly, negative linear DOP values (red-shaded pixels) signify relatively higher co-linear intensity compared to cross-linear intensity, according to Equation (4).

For circular polarization, as hypothesized and as previously shown,[1,8,20,12,63–65] helicity-flipping intensity increases relative to helicity-preservation intensity as scatterer size decreases (the proportion of negative pixels increases going from Figure 5 (a) to (b) to (c)). This occurs due to enhanced backward-scattering from the spheres as they decrease in size (e.g., notice that, in single scattering, there is proportionally more backward-scattering in Figure 2b compared to Figure 2f), giving rise to increased type-1 backscattering (i.e., mirror-like reflections from scatterers) and hence helicity-flipping. Additionally, helicity-flipping is most prominent closer to the incident beam-spot whereas helicity-preservation is most prominent outside of the incident beamspot, as was depicted and hypothesized in Figure 3c.

For linear polarization, there is more co-linear intensity than cross-linear intensity as sphere size decreases (the proportion of negative pixels increases going from Figure 5 (d) to (f), as previously observed.[8,10,49,50,51] Similar to the circular polarization case, this is due to the enhanced backward-scattering as spheres decrease in size – notice that there is proportionally more backward-scattering in Figure 2d compared to Figure 2h – giving rise to increased type-1 backscattering and hence more co-linear polarization. However, unlike the circular polarization case, the linear DOP images are not rotationally symmetrical, instead, they exhibit lobed patterns of positive and negative values, as previously observed.[56,59–62] These lobes arise from geometrical re-orientation of the linear polarization vectors to either co-linear states (negative linear DOP values) or cross-linear states (positive linear DOP values) as described and hypothesized in Figure 4. Importantly, notice that the co-linear intensity increases along the axis that is perpendicular to the incident linear vertical polarization vector as sphere size decreases (e.g., see the prominent horizontal band of negative / red-coloured pixels in Figure 5f). This is directly related to the enhanced isotropic scattering along the perpendicular plane for linearly polarized light (the X-Y plane in Figure 2c,d) which gives rise to type-1 backscattering along this plane in addition to type-2 backscattering – both of which yield co-linear polarization. Therefore, since co-linear polarization is enhanced by both types of backscattering, whereas helicity-flipped light is only enhanced by type-1 backscattering, co-linear polarization "outcompetes" helicity-flipped circular polarization. This gives rise to a higher co-linear-to-cross-linear intensity than helicity-flipping-to-helicity-preserved intensity for the Rayleigh scatterers (0.03 μm spheres), which is visually apparent upon comparison between Figure 5c and f. According to Equations (2) and (4), higher co-linear-to-cross-linear intensity than helicity-flipping-to-helicity-preserved intensity implies that linear DOP will be higher than circular DOP (in magnitude), since $|\perp - \parallel| > |HP - HF|$, thereby yielding $|\,\mathrm{DOLP}\,| > |\,\mathrm{DOCP}\,|$.

As an interesting aside, notice in Figure 5d,e that there is slightly more co-linear intensity along the perpendicular axis (the horizontal axis). Upon examination of the linear polarization single-scattering plot for the 1.04 μm sphere in Figure 2h, it appears that there is somewhat higher scattering intensity in the backward hemisphere in the perpendicular plane (X-Z plane) than in the parallel plane (X-Y plane). Thus, the increased co-linear intensity along the perpendicular axis of Figure 5d and e likely arises from the slightly increased back-scattering intensity along the perpendicular plane. In our previous study,[56] we noticed this "oblong" skew to the four-lobed pattern along the perpendicular axis which we did not yet understand; this provides some exploratory insights into these observations.

Figure 6 shows the simulation-obtained average linear DOP (denoted as 'DOCP') and circular DOP (denoted as 'DOCP') values for five different microsphere suspensions with sphere diameters (bottom axis) of 0.03, 0.20, 0.50, 0.75, and 1.04 μm, and each suspension with a matched reduced scattering coefficient

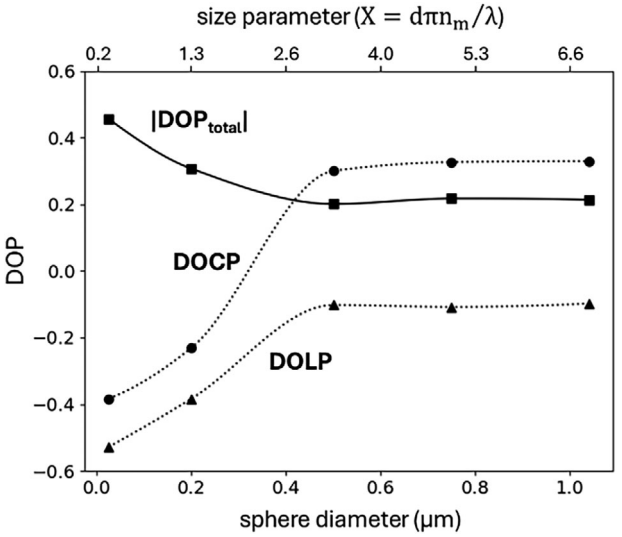

Figure 6. Simulated linear DOP ('DOLP') and circular DOP ('DOCP') for different microsphere diameters; the corresponding size parameter (X) for each sphere diameter is shown on the top axis. DOP values are calculated by averaging each pixel in the simulated DOP image of backscattered light from a microsphere suspension (each with $\mu_s' = 3.4\ cm^{-1}$). The entire surface of each microsphere suspension was illuminated by linearly polarized light (for linear DOP calculations) or circularly polarized light (for circular DOP). The total DOP, | DOP_{total} | , is calculated as the average of | DOLP | and | DOCP |. The lines are guides for the eye.

of $\mu_s' = 3.4\ cm^{-1}$. Also, the corresponding size parameter (X) for each sphere diameter is shown on the top axis of Figure 6, calculated as: $X = d\pi n_m/\lambda$, where d is sphere diameter, n_m is the host medium refractive index (1.33), and λ is the illumination wavelength (632.8 nm). The total DOP, | DOP_{total} |, is also shown and is calculated by taking the average of | DOLP | and | DOCP |. Note that each of these DOP values are obtained from wide-field illumination images, whereby the entire suspension is illuminated (as opposed to pencil-beam illumination in Figure 5) by either circular polarization or linear vertical polarization; the circular and linear DOP values are calculated by summing the DOP value of each pixel of the linear or circular DOP image, then dividing by the number of pixels. Central beam-spot illumination is useful for understanding backscattering pathways, as was shown in Figure 5, however, we choose to compare DOP data from wide-field illumination images since many imaging applications illuminate the entire sample.

As expected for the Rayleigh-like 0.03 μm spheres, it is seen that linear DOP is higher in magnitude than circular DOP; both linear DOP and circular DOP are negative due to the higher co-linear-to-cross-linear intensity and higher helicity-flip-to-helicity-preserve intensity, respectively (see Equations (2) and (4)). This behaviour is also seen in the 0.20 μm sphere suspension. As the sphere diameters increase to the non-Rayleigh regime (sphere diameter ≈ λ and greater) of 0.50, 0.75, and 1.04 μm spheres, the trend reverses and circular DOP becomes greater in magnitude than linear DOP as expected; however, linear DOP remains negative. Notice that | DOP_{total} | is highest for the Rayleigh-regime 0.03 μm spheres. Therefore, it is seen that small Rayleigh-regime scatterers increase linear DOP versus circular DOP due to the higher co-linear-to-cross-linear intensity compared to the helicity-flipped-to-helicity-preserved intensity. Co-linear intensity outcompetes its helicity-flipped counterpart in this regime, since it is brought about by *both* type-1 backscattering and type-2 backscattering in the perpendicular plane, whereas helicity-flipping is only supported by type-1 backscattering.

Interestingly, in bio-polarimetry it has often been observed that 1) the total DOP is higher in cancerous tissues compared to normal tissues [66–71] for which the underlying reasons are not yet well understood. Additionally, cancerous tissues have been observed to exhibit 2) higher helicity-flipping intensity compared to helicity-preserved intensity, 3) higher co-linear intensity compared to cross-linear intensity, and (4) higher linear DOP than circular DOP.[29,36,69,72,73,74] In this study, the findings in Figure 6 show that the above-noted observations (1–4) are each associated with small-sized Rayleigh-regime scattering media. Specifically, notice that the suspension comprised of 0.03 μm spheres yields a higher total DOP, highly negative circular DOP (indicating preponderance of helicity-flipping), highly negative linear DOP (indicating preponderance of co-linearity), and higher linear DOP compared to circular DOP; see our recent study for details on this subject.[75] Since these Rayleigh-associated polarimetric signatures are observed in malignant tissues, it may indicate that malignant tissues contain more small-sized Rayleigh-regime scatterers (e.g., possibly due to increased cell density and hence higher concentrations of mitochondria,[76] and/or cellular fragments due to apoptosis and other cancer-related processes).[77] If malignant tissues are indeed comprised of more small-sized Rayleigh-regime scatterers in comparison to healthy tissue, it may be the reason why malignant tissues are commonly observed to have higher DOPs than healthy tissue [66–71] (since small-sized scattering turbid media appear to yield higher DOP values, as exhibited by the 0.03 μm spheres in Figure 6). Future work should further explore the linkage between scatterer size and polarimetric responses, particularly in the complex milieu of biological tissues.

4. Summary and Conclusion

In this study, through experimental measurements and computational modeling, it is found that single-scattering directionality directly influences multiple-scattering pathways of light in turbid heterogeneous media. Importantly, since the size of single scatterers greatly modulates single scattering directionality, it also modulates the types of multiple-scattering pathways which light undergoes before re-emerging from a medium. It is shown that there are two prominent types of pathways, which we refer to as 'type-1' and 'type-2'; the former describes light which undergoes a mirror-like large angle reflection by a scatterer, abruptly re-directing light into the backward hemisphere of the medium, and the latter describes light which takes an arc-like pathways via near-forward scattering events (i.e., no mirror-like reflection event). The relative proportions of each of these backscattering pathway types appear to govern the amount of helicity-flipped/co-linear polarization and helicity-preserved/cross-linear polarization, which in turn determine the circular DOP and linear DOP values. Therefore, scatterer size seems to modulate DOP values through a cascade of effects: first influencing single-scattering directionality, which then influences multiple-scattering pathways,

which then influences the relative fractions of parallel and perpendicular circular and linear polarization states, which then (finally) governs circular and linear DOP values.

The results of the study show that linear DOP becomes greater in magnitude than circular DOP for Rayleigh-sized scatterers due to the higher co-linear-to-cross-linear intensity for linear incidence compared to the helicity-flipped-to-helicity-preserved intensity for circular incidence. This difference in linear and circular polarization intensities arises from the disproportionate enhancement of co-linear intensity as scatterer sizes enter the Rayleigh regime which gives rise to increased probabilities of type-1 scattering in addition to type-2 scattering along the plane perpendicular to the incident linear polarization vector. These ratios, co-linear-to-cross-linear or helicity-flipped-to-helicity-preserved intensities, are tracked through the use of modified signed Stokes DOP formulas (Equations (2) and (4)), which encode negative values to indicate a preponderance of co-linear or helicity-flipped intensity, whilst maintaining the same magnitude that would be measured through the conventional Stokes DOP calculations.

These findings on why and how linear and circular DOPs can differ in turbid media may aid in the interpretation of empirical observations often reported in the bio-polarimetry literature, particularly as it pertains to how depolarization occurs in malignant versus healthy tissue. However, the linkage and translatability between phantoms (such as those employed in this study) and actual biological tissue requires further research. Importantly, it must be pointed out that scatterer size is just one of many properties in biological tissues which may undergo changes as disease progresses; thus it is important to explore polarimetric responses to other tissue/medium property changes such as to heterogeneity, turbidity, refractive index, and absorption. In particular, a controlled study on the effects of absorption may lend important insight into type-1 and type-2 backscattering, since absorption extinguishes longer pathlength / deeply penetrating light.[65,78] We may thus posit that type-2 backscattering intensity will decrease more than that of type-1 backscattering in the presence of absorption, since type-2 backscattered light exhibits longer pathlengths.[55]

It should also be noted that illumination-detection geometry is an important issue to further explore as the experimental requirements – such as, space constraints, beam-splitter versus no beam-splitter configurations, signal intensity and measurement times, etc. – vary and can influence the polarimetric findings. For example, some researchers perform polarimetry whereby the detection axis forms an oblique angle with the incident beam (backscattering hemisphere direction), as opposed to the *en-face* retro-reflection configuration (exact backscattering direction) used in this study. These differences will likely result in slightly different subsurface photon paths as we demonstrated previously with Monte Carlo simulations.[79] For example, type-1 mirror-like large-angle backscattering photons may re-emerge from a medium nearly parallel to the illumination beam, possibly resulting in lower type-1 intensity if measured in the off-backscattering-axis detector geometry (e.g., outside the field of view of the detector). A better understanding of these geometry-dependent effects could enable robust identification of 'optimum' configuration(s) based on practical requirements.

Finally, it would be useful to directly track the number of type-1 and type-2 photons using the Monte Carlo simulation platform. This will lend further insight into the depolarization mechanisms of linear and circular states and the role of type-1 and type-2 backscattering pathways. The Monte Carlo platform employed in this study is not currently able to directly track these statistics; instead, we infer the backscattering pathways based on polarimetric signatures. For example, it was shown in our previous study[55] that the number of helicity-flipped photons can be used as an indirect measure of type-1 population, since helicity-flipping occurs upon a mirror-like, large-angle reflection from a scatterer. Analogously, the number of helicity-preserved photons can be used to infer the type-2 cohort since these do not undergo large-angle back-reflection events. Also, the role of the photons which undergo a combination of several mirror-like reflection and forward-scattering events is not yet fully understood; we posit that these can be considered background noise since they become depolarized (i.e., they do not have a preferential polarization state and hence have an equal probability to exhibit right- / left-handed circular polarization or co- / crossed-linear polarization). To test this and gain further insight into these polarization-pathlength relationships, we are pursuing a follow-up study which employs a Monte Carlo to directly track these statistics.

Acknowledgements

The authors kindly acknowledge the funding sources: Canadian Institutes of Health Research (CIHR, PJT-156110), the Natural Sciences and Engineering Research Council of Canada (RGPIN-2018-04930), and the New Frontiers in Research Fund (NFRFE-2019-01049).

Conflict of Interest

The authors declare no conflicts of interest.

Data Availability Statement

The data that support the findings of this study are available from the corresponding author upon reasonable request.

Keywords

biophotonics, cancer detection, depolarization, mie scattering, rayleigh scattering, scatterer size, tissue polarimetry

Received: June 13, 2025
Revised: August 26, 2025
Published online:

[1] D. Bicout, C. Brosseau, A. S. Martinez, J. M. Schmitt, *Phys. Rev. E* **1994**, *49*, 1767.
[2] C. Brosseau, Fundamentals of Polarized Light, Wiley-Interscience, USA **1998**, p. 118.
[3] C. F. Bohren, D. R. Huffman, Absorption and Scattering of Light by Small Particles, Wiley, **1998**.
[4] A. P. Minton, *Anal. Biochem.* **2016**, *501*, 4.

[5] N. Palmer, R. von Wandruszka, *Fresenius J Anal Chem* **2001**, *371*, 951.
[6] R. S. Gurjar, V. Backman, L. T. Perelman, I. Georgakoudi, K. Badizadegan, I. Itzkan, R. R. Dasari, M. S. Feld, *Nat. Med.* **2001**, *7*, 1245.
[7] V. Backman, M. B. Wallace, L. T. Perelman, J. T. Arendt, R. Gurjar, M. G. Müller, Q. Zhang, G. Zonios, E. Kline, T. McGillican, S. Shapshay, T. Valdez, K. Badizadegan, J. M. Crawford, M. Fitzmaurice, S. Kabani, H. S. Levin, M. Seiler, R. R. Dasari, I. Itzkan, J. Van Dam, M. S. Feld, *Nature* **2000**, *406*, 35.
[8] F. C. MacKintosh, J. X. Zhu, D. J. Pine, D. A. Weitz, *Phys. Rev. B* **1989**, *40*, 9342.
[9] J. M. Schmitt, A. H. Gandjbakhche, R. F. Bonner, *Appl. Opt.* **1992**, *31*, 6535.
[10] X. Ni, R. R. Alfano, *Opt. Lett.* **2004**, *29*, 2773.
[11] M. Xu, R. R. Alfano, *Phys. Rev. Lett.* **2005**, *95*, 213901.
[12] M. Xu, R. R. Alfano, *Phys. Rev. E* **2005**, *72*, 065601.
[13] V. Kuzmin, I. Meglinski, in Biomedical Applications of Light Scattering IV (Eds: A. P. Wax, V. Backman), p. 75730Z.
[14] N. Ghosh, P. K. Gupta, H. S. Patel, B. Jain, B. N. Singh, *Opt. Commun.* **2003**, *222*, 93.
[15] A. D. Kim, M. Moscoso, *Phys Rev E Stat Phys Plasmas Fluids Relat Interdiscip Topics* **2001**, *64*, 5.
[16] E. E. Gorodnichev, A. I. Kuzovlev, D. B. Rogozkin, *JETP Lett.* **1998**, *68*, 22.
[17] A. D. Kim, M. Moscoso, *Opt. Lett.* **2002**, *27*, 1589.
[18] Y. L. Kim, P. Pradhan, M. H. Kim, V. Backman, *Opt. Lett.* **2006**, *31*, 2744.
[19] M. J. Raković, G. W. Kattawar, M. Mehrűbeoğlu, B. D. Cameron, L. V. Wang, S. Rastegar, G. L. Coté, *Appl. Opt.* **1999**, *38*, 3399.
[20] M. D. Singh, I. A. Vitkin, *Biomed. Opt. Express* **2021**, *12*, 6831.
[21] E. E. Gorodnichev, A. I. Kuzovlev, D. B. Rogozkin, *J. Exp. Theor. Phys.* **2008**, *106*, 731.
[22] E. E. Gorodnichev, A. I. Kuzovlev, D. B. Rogozkin, *Phys. Rev. E* **2014**, *90*, 043205.
[23] F. C. MacKintosh, S. John, *Phys. Rev. B* **1989**, *40*, 2383.
[24] C. He, H. He, J. Chang, B. Chen, H. Ma, M. J. Booth, *Light Sci Appl* **2021**, *10*, 194.
[25] M. D. Singh, N. Ghosh, I. A. Vitkin, in *Polarized Light in Biomedical Imaging and Sensing* (Eds: J. C. Ramella-Roman, T. Novikova), Springer International Publishing, Cham, **2023**, pp. 61–103.
[26] M. Ahmad, S. Alali, A. Kim, M. F. G. Wood, M. Ikram, I. A. Vitkin, *Biomed. Opt. Express* **2011**, *2*, 3248.
[27] A. Cerussi, N. Shah, D. Hsiang, A. Durkin, J. Butler, B. J. Tromberg, *J. Biomed. Opt.* **2006**, *11*, 044005.
[28] A. Garcia-Uribe, E. B. Smith, J. Zou, M. Duvic, V. Prieto, L. V. Wang, *J. Biomed. Opt.* **2011**, *16*, 020501.
[29] T. Novikova, A. Pierangelo, S. Manhas, A. Benali, P. Validire, B. Gayet, A. De Martino, *Appl. Phys. Lett.* **2013**, *102*, 241103.
[30] J. Wang, W. Zheng, K. Lin, Z. Huang, *Biomed. Opt. Express* **2016**, *7*, 1116.
[31] D. Ivanov, V. Dremin, E. Borisova, A. Bykov, T. Novikova, I. Meglinski, R. Ossikovski, *Biomed. Opt. Express* **2021**, *12*, 4560.
[32] D. Louie, L. Tchvialeva, S. Kalia, H. Lui, T. Lee, *Biomed. Opt. Express* **2021**, *13*, 620.
[33] N. Nishizawa, T. Kuchimaru, *J Biophotonics* **2022**, *15*, 202200062.
[34] L. T. Perelman, V. Backman, M. Wallace, G. Zonios, R. Manoharan, A. Nusrat, S. Shields, M. Seiler, C. Lima, T. Hamano, I. Itzkan, J. Van Dam, J. M. Crawford, M. S. Feld, *Phys. Rev. Lett.* **1998**, *80*, 627.
[35] V. Backman, R. Gurjar, K. Badizadegan, I. Itzkan, R. R. Dasari, L. T. Perelman, M. S. Feld, *IEEE J. Sel. Top. Quantum Electron.* **1999**, *5*, 1019.
[36] M.-R. Antonelli, A. Pierangelo, T. Novikova, P. Validire, A. Benali, B. Gayet, A. De Martino, *Opt. Express* **2010**, *18*, 10200.
[37] T. Novikova, A. Pierangelo, A. De Martino, A. Benali, P. Validire, *Opt Photonics News* **2012**, *23*, 26.
[38] V. Sankaran, J. T. Walsh, D. J. Maitland, *J. Biomed. Opt.* **2002**, *7*, 300.
[39] A. Pierangelo, S. Manhas, A. Benali, C. Fallet, M.-R. Antonelli, T. Novikova, B. Gayet, P. Validire, A. De Martino, *J. Biomed. Opt.* **2012**, *17*, 066009.
[40] I. Myserlis, E. Angelakis, A. Kraus, C. A. Liontas, N. Marchili, M. F. Aller, H. D. Aller, V. Karamanavis, L. Fuhrmann, T. P. Krichbaum, J. A. Zensus, *Astron Astrophys* **2018**, *609*, A68.
[41] S. Morgan, M. Ridgway, *Opt. Express* **2000**, *7*, 395.
[42] A. D. Kim, S. Jaruwatanadilok, A. Ishimaru, Y. Kuga, *Laser-Tissue Interaction XII: Photochemical, Photothermal, and Photomechanical* **2001**, *4257*, 90.
[43] M. D. Singh, L. A. Ye, M. Woolman, F. Talbot, A. Zarrine-Asfar, A. Vitkin, *Sci. Rep.* **2024**, *14*, 26230.
[44] A. Pierangelo, A. Nazac, A. Benali, P. Validire, H. Cohen, T. Novikova, B. H. Ibrahim, S. Manhas, C. Fallet, M.-R. Antonelli, A.-D. Martino, *Opt. Express* **2013**, *21*, 14120.
[45] E. Du, H. He, N. Zeng, Y. Guo, M. Sun, H. Ma, S. Liu, M. Li, *Advanced Biomedical and Clinical Diagnostic Systems XII* **2014**, *8935*, 89350S.
[46] J. C. Ramella-Roman, I. Saytashev, M. Piccini, *J. Opt.* **2020**, *22*, 123001.
[47] S. G. Demos, H. Savage, A. S. Heerdt, S. Schantz, R. R. Alfano, *Opt. Commun.* **1996**, *124*, 439.
[48] S. G. Demos, R. R. Alfano, *Opt. Lett.* **1996**, *21*, 161.
[49] S. A. Kartazayeva, X. Ni, R. R. Alfano, *Opt. Lett.* **2005**, *30*, 1168.
[50] M. Sakami, A. Dogariu, *Journal of the Optical Society of America A* **2006**, *23*, 664.
[51] M. Hornung, A. Jain, M. Frenz, H. G. Akarçay, *Opt. Express* **2019**, *27*, 6210.
[52] C. F. Bohren, D. R. Huffman, in *Absorption and Scattering of Light by Small Particles*, Wiley-VCH Verlag GmbH, Weinheim, Germany, **2007**, pp. 82–129.
[53] H. C. van de Hulst, Light Scattering by Small Particles, Dover Publications, **1981**.
[54] S. Prahl, "Mie Scattering Calculator," https://omlc.org/calc/mie_calc.html (accessed: 2025), **2023**.
[55] M. D. Singh, I. A. Vitkin, *Sci. Rep.* **2023**, *13*, 2231.
[56] M. D. Singh, L. Lilge, A. Vitkin, *J. Biomed. Opt.* **2023**, *28*, 102906.
[57] H. C. van de Hulst, in Light Scattering by Small Particles, Dover Publications, **1981**, pp. 63–66.
[58] H. C. van de Hulst, *Light Scattering by Small Particles*, Dover Publications, USA, **1981**, pp. 88.
[59] Y. Kuga, L. Tsang, A. Ishimaru, *Journal of the Optical Society of America A* **1985**, *2*, 616.
[60] M. Dogariu, T. Asakura, *J. Opt.* **1993**, *24*, 271.
[61] M. Dogariu, *Optical Engineering* **1996**, *35*, 2234.
[62] A. H. Hielscher, J. R. Mourant, I. J. Bigio, *Appl Opt.* **1997**, *36*, 125.
[63] V. Kuzmin, I. Meglinski, in Biomedical Applications of Light Scattering IV (Eds: A. P. Wax, V. Backman), **2010**, p. 75730Z.
[64] C. M. Macdonald, S. L. Jacques, I. V. Meglinski, *Phys. Rev. E* **2015**, *91*, 033204.
[65] C. A. Nader, R. Nassif, F. Pellen, B. Le Jeune, G. Le Brun, M. Abboud, *Appl. Opt.* **2015**, *54*, 10369.
[66] M. H. Smith, P. D. Burke, A. Lompado, E. A. Tanner, L. W. Hillman, in Biomedical Diagnostic, Guidance, and Surgical-Assist Systems II (Eds: T. Vo-Dinh, W. S. Grundfest, D. A. Benaron), **2000**, pp. 210–216.
[67] M. Anastasiadou, A. De Martino, D. Clement, F. Liège, B. Laude-Boulesteix, N. Quang, J. Dreyfuss, B. Huynh, A. Nazac, L. Schwartz, H. Cohen, *physica status solidi* **2008**, *5*, 1423.

[68] S. Firdous, S. Anwar, *Optik (Stuttg)* **2016**, *127*, 3035.
[69] D. Ivanov, V. Dremin, A. Bykov, E. Borisova, T. Genova, A. Popov, R. Ossikovski, T. Novikova, I. Meglinski, *J Biophotonics* **2020**, *13*, 1.
[70] J. Chung, W. Jung, M. J. Hammer-Wilson, P. Wilder-Smith, Z. Chen, *Appl Opt.* **2007**, *46*, 3038.
[71] J. Qi, T. Tatla, E. Nissanka-Jayasuriya, A. Y. Yuan, D. Stoyanov, D. S. Elson, *Nat. Biomed. Eng.* **2023**, *7*, 971.
[72] J. R. Mourant, A. H. Hielscher, A. A. Eick, T. M. Johnson, J. P. Freyer, *Cancer* **1998**, *84*, 366.
[73] A. Hielscher, A. Eick, J. Mourant, D. Shen, J. Freyer, I. Bigio, *Opt. Express* **1997**, *1*, 441.
[74] J. Ramachandran, T. M. Powers, S. Carpenter, A. Garcia-Lopez, J. P. Freyer, J. R. Mourant, *Opt. Express* **2007**, *15*, 4039.
[75] M. D. Singh, H. A. Contreras-Sánchez, I. A. Vitkin, *J. Biomed. Opt.* **2025**, *30*, S34105.
[76] H. Fang, M. Ollero, E. Vitkin, L. M. Kimerer, P. B. Cipolloni, M. M. Zaman, S. D. Freedman, I. J. Bigio, I. Itzkan, E. B. Hanlon, L. T. Perelman, *IEEE Journal on Selected Topics in Quantum Electronics* **2003**, *9*, 267.
[77] C. S. Mulvey, C. A. Sherwood, I. J. Bigio, *J. Biomed. Opt.* **2009**, *14*, 064013.
[78] I. A. Vitkin, R. C. N. Studinski, *Opt. Commun.* **2001**, *190*, 37.
[79] X. Guo, M. F. G. Wood, A. Vitkin, *Opt. Express* **2007**, *15*, 1348.